Evolution in microstructure and properties during non-isothermal annealing of a cold-rolled Al-Mn-Fe-Si alloy with different microchemistry states

K. Huang[a], O. Engler[b], Y.J. Li[a], K. Marthinsen[a]

[a] Department of Materials Science and Engineering, Norwegian University of Science and Technology, Trondheim, N-7491 Trondheim, Norway

[b] Hydro Aluminium Rolled Products, Research and Development Bonn, D-53014 Bonn, Germany

Abstract

The softening behaviour during non-isothermal annealing of a cold-rolled Al-Mn-Fe-Si model alloy was studied as a function of the state of microchemistry, in terms of the solute level of Mn, size and spatial distribution of the Mn-bearing dispersoids, as well as their temporal evolution. Microchemistry significantly affects the recrystallization microstructure, crystallographic texture as well as the mechanical property of the investigated alloy after non-isothermal annealing. The nucleation and growth of grains with different orientations are strongly dependent on both annealing temperature and microchemistry, in that pre-existing dispersoids have a less profound effect on retarding recrystallization than dispersoids forming concurrently during back-annealing. Strong concurrent precipitation suppresses nucleation and retards recrystallization, which finally leads to a coarse and pan-cake shaped grain structure, accompanied by strong P $\{011\}<566>$ and/or M $\{113\}<110>$ texture components and a relatively weaker ND-rotated cube $\{001\}<310>$ component. A refined grain structure with medium strength P and cube $\{001\}<100>$ components is obtained when the pre-existing dispersoids are coarser and fewer, and concurrent precipitation is limited. P-orientated grains are less affected by second phase particles and experience a growth advantage at low annealing temperatures ($<350°C$), while M-orientated grains appear at higher temperatures. The intensity of the P texture does not necessarily increase with increasing supersaturation of Mn as observed during isothermal annealing, whereas the level of supersaturated Mn promotes the strength of the M texture. The mechanisms behind are discussed.

Key words: Aluminium alloy; Recrystallization; Particles; Texture; Precipitation; Non-isothermal annealing

1. Introduction

It is well established that second phase particles in a metallic material have a strong influence on the recrystallization behaviour [1-5]. Fine dispersoids exert a pinning effect on both high and low angle boundaries [6,7], where a broader size distribution of fine dispersoids leads to a larger effective Zener drag pressure [8]. Coarse particles (>1μm), typically formed during casting, may provide sites for particle stimulated nucleation (PSN) and thus accelerate recrystallization [9], in contrast. Aluminium alloys of the AA3xxx-series contain Mn as their main alloying element, while elements like Fe, Si, Mg and Cu often are added to obtain desired mechanical properties. Besides, these elements may also accumulate unintentionally in secondary alloys after recycling. In any case the microstructural evolution and associated mechanical properties may be strongly affected during processing. During the solidification of AA3xxx alloys, most of the Fe content forms intermetallic constituent particles while the majority of Mn content remains in solid solution, leading to supersaturation of the solid solution. The supersaturated Mn will precipitate as Mn-bearing dispersoids during subsequent thermo-mechanical processing steps [10-13], thus changing the microchemistry of the alloy [14].

The effect of microchemistry, in terms of solute level of Mn and the distribution of second phase particles, on the softening behaviour of AA3xxx aluminium alloys during isothermal annealing has been studied extensively, e.g. [14-19]. However, the influence of *non-isothermal* heat treatments on microstructure and texture evolution is much less documented as compared to its counterpart isothermal annealing [20-22]; moreover, the effect of microchemistry changes during non-isothermal annealing is often left unexplored, e.g. [23]. Liu *et al.* [22] studied the annealing behaviour of commercially produced hot band of a continuously cast AA3105 alloy using two different heating rates. Coarse elongated recrystallized grains were observed after annealing to and holding for 6h at temperatures of 482-599°C with a relatively strong P {011}<566> texture component and a 22.5° ND-rotated cube {001}<310> component at the lower heating rate. The effect of microchemistry on the microstructural evolution was not addressed, however.

Schäfer and Gottstein found that the P texture becomes more pronounced for low heating rates, when precipitation of dispersoids occurs prior to or concurrently with recrystallization [24]. The effect of heating rate on the evolution of microstructure and final recrystallized grain size in two Al-Zn-Mg-Cu alloys was analysed by Bampton *et al.* [25], but in their work the recrystallization texture evolution was not considered.

During isothermal annealing, the intensity of the P texture was found to increase with increasing initial cold rolling reduction, increasing initial supersaturation of Mn, and decreasing annealing temperature [18]. Besides the P texture, a new M {113}<110> recrystallization texture component has been obtained in a supersaturated Al-Mn alloy, both of which increase in intensity at low annealing temperatures during isothermal annealing [26]. A recent investigation on the recrystallization microstructures and textures forming after non-isothermal annealing has demonstrated that a large number of fine dispersoids together with strong concurrent precipitation lead to a coarse and pan-cake shaped grain structure with strong P and ND-rotated cube texture components [23]. However, detailed investigations on the gradual microstructural evolution during non-isothermal annealing, taking into account the effect of different microchemistries, have not been

conducted to date. During non-isothermal heat treatments of Al-Mn alloys both recovery and concurrent precipitation of dispersoids are likely to occur, producing complex interactions with recrystallization [21]. Unlike isothermal annealing, where the effect of concurrent precipitation can mainly be avoided at high temperatures since recrystallization kinetics is very fast, the dispersoids precipitated at lower temperatures will inevitably affect the softening behaviour at higher temperatures during non-isothermal annealing. It is also possible to analyse how temperature affect the nucleation and growth of grains with different orientations during non-isothermal annealing. It is thus of great interest to investigate the microstructural evolution during non-isothermal annealing of cold-deformed particle containing aluminium alloys.

The main objective of the present work has been to establish a better understanding and to document the effect of microchemistry, in terms of solute level of Mn and the distribution of second phase particles, on grain structure, recrystallization texture as well as mechanical properties of a cold-rolled Al-Mn-Fe-Si model alloy during and after non-isothermal annealing. In the first part, the experimental details on different homogenization procedures, cold rolling and subsequent annealing are given, as well as the microstructure characterization methods utilized. In the second part, the experimental results on microstructural evolution during non-isothermal annealing are presented. A careful discussion of the experimental results and their possible interpretations is provided in the last part.

2. Experimental

The examined samples were machined from the central region of a direct chill (DC) cast AA3xxx-type alloy extrusion billet of 288 mm in diameter, supplied by Hydro Aluminium in Norway. The as-received material was in the as-cast state, with the chemical composition (in wt.%) of 0.152% Si, 0.530% Fe, 0.390% Mn with Al balance. More detailed information on the as-received material can be found elsewhere [14].

The samples in as-cast states were homogenized at two different conditions to achieve desired levels of Mn in solid solution and, in turn, different densities of dispersoid particles. To be consistent with previous work on the same set of alloys [14,23,27,28], the two homogenized materials were labelled as C1-2 and C1-3, respectively. The homogenization treatments were all performed in an air circulation furnace with a temperature accuracy of ± 2 °C, starting from room temperature (about 20 °C). The first set of samples, hereafter referred to as C1-2, was heated with a constant heating rate of 50 K/h to 450 °C and kept for 4 hours. The second set of samples (C1-3) was subjected to a two-stage homogenization treatment: these samples were first heated at 50 K/h to 600 °C, held for 4 hours, and then cooled at 25 K/h to 500°C where they were kept for another 4 hours. After homogenization, the samples were water quenched to room temperature to freeze the state of supersaturation/precipitation.

In addition to the two homogenized variants, the as-cast condition, which is designated as C1-0, was also included in the study, giving a total of three different initial solid solution levels of Mn. These three variants were all rolled at room temperature by multiple passes to an accumulated deformation strain of $\varepsilon = 3.0$. The cold rolled sheets were then heated at 50 K/h in an air circulation

furnace to different prescribed temperatures in the range of 100-500 °C, to follow the microstructural evolution upon non-isothermal annealing. Once the samples reached the desired temperature, they were water quenched without any significant holding time. On the other hand, some of the samples were kept at the desired temperature for periods of up to 10^5s.

The microstructure characterization details have already been described in detail elsewhere [14], so only some key information will be reiterated here to increase the readability. Both hardness and electrical conductivity measurements were performed on the RD-TD plane of the samples in order to follow the softening and precipitation behaviours during annealing. Each reported value was obtained by averaging eight measurements at different positions on the RD-TD plane of the examined samples. A load of 1 Kg, a dwell time of 15s and a loading speed of $100\mu ms^{-1}$ were used for the hardness measurements. Electrical conductivity was measured by a Sigmascope EX 8 instrument at room temperature of about 293 K (20°C). The mechanical behaviour of the three variants, non-isothermally heated to 400°C and kept for 10^5s after cold rolling to ε=3.0, was also analysed by tensile tests. For that purpose standard tensile test specimens were machined with the tensile direction being parallel to the rolling direction and tested at room temperature with a nominal strain rate of $\sim 10^{-3}s^{-1}$.

Metallographic examinations of constituent particles and dispersoids were performed by backscattered electrons (BSE) in a Zeiss Supra 55 field emission gun scanning electron microscope (FEG-SEM). Images were recorded electronically and analysed in terms of characteristic size parameters of constituent particles and dispersoids, viz. equivalent diameter *d* and number density using the standard image analysis software Image-J. The crystallographic textures of the sheets were measured by means of electron backscatter diffraction (EBSD) on the same Zeiss Supra 55 scanning electron microscope (SEM) using the TSL OIM^{TM} Data Analysis 6 software from EDAX, Inc. EBSD orientation maps of the annealed samples, with more than one thousand grains (except for the cases with extremely large grains), were obtained to study the orientation of the recrystallized grains and thus the texture evolution during recrystallization. For all the micrographs presented in this study, the horizontal direction corresponds to the rolling direction (RD) while the vertical direction is the normal direction (ND).

A selection of conditions is presented in this paper such as to illustrate the evolution of the microstructure during annealing. The grain size was determined as the equivalent circular diameter in the RD-ND cross section. Recrystallized grains were identified as those being partly or fully surrounded by a high-angle boundary (>15°), with grain size larger than 3 times the scanning step size and with interior misorientations below 2° [29]. The texture is represented in terms of orientation distribution functions (ODFs) by imposing orthotropic (rolling) sample symmetry, and using the harmonic series expansion method (L=22) with a Gaussian half-width of 5° [30]. If the observed grain orientation was within a 15° scatter (in all directions) from the ideal texture components, it was classified as belonging to that specific component, including {112}<111> (Cu), {124}<211> (R) and {123}<634> (S), {110}<112> (Bs), {001}<100> (cube), {113}<110> (M) [26] and {001}<310> (ND-rotated cube). It should be noted that for the {011}<566> (P) component, slightly different definitions are also used in the literature, e.g. {110}<111> [**Error! Bookmark not defined.,Error! Bookmark not defined.**], {110}<455> [31], or {110}<122> [32]. Since the P component may overlap with the nearby Bs component, a smaller scatter of 10° is applied for the detection of the former. Remaining orientations are summarized as "other orientations".

3. Results
3.1. Microchemistry states before back-annealing

The microchemistry state of the as-cast and the two differently homogenized conditions is summarized in Table 1. The as-cast variant, C1-0, possesses no pre-existing dispersoids, but has the highest concentration of Mn in solid solution. For the condition homogenized at a high temperature (C1-3), the constituent particles are slightly coarser (larger but lower number density) compared to both the as-cast variant (C1-0) and the sample homogenized at a lower temperature (C1-2). This is characteristic of a coarsening of the constituent particles during homogenization at high temperatures. On the other hand, more and finer dispersoids, randomly distributed, are observed for C1-2 [14], as seen from the values of diameter and number density of dispersoids reported in Table 1. The C1-2 variant shows a lower electrical conductivity than C1-3, reflecting a higher supersaturation of Mn in solid solution in the former material and thus a higher potential for precipitation of Mn-containing dispersoids during subsequent annealing. The solid solution level of Mn was estimated based on the relationship between the conductivity and concentration of alloying elements in solid solution, details of which can be found in Ref. [12,23].

Table 1. Electrical conductivity, concentrations of solutes, diameter and number density of particles in the alloys studied [14]

	Electrical conductivity (m/Ωmm^2)	Concentration of Mn (wt%)	Constituent particles		Dispersoids	
			Diameter (µm)	Number density (mm^{-2})	Diameter (µm)	Number density (mm^{-2})
C1-0	23.9	0.35	0.88	$2.8 \cdot 10^4$	-	-
C1-2	27.5	0.16	0.96	$2.9 \cdot 10^4$	0.054	$1.3 \cdot 10^6$
C1-3	29.0	0.11	1.10	$2.1 \cdot 10^4$	0.127	$5.5 \cdot 10^4$

3.2. Influence of microchemistry on microstructure, texture and mechanical properties

It has recently been documented that the recrystallization microstructure and texture during isothermal annealing of Al-Mn-Fe-Si alloys are strongly affected by the microchemistry state [14]. In the present study, the effect of microchemistry on recrystallization structure and texture, as well as the mechanical properties has been examined after *non-isothermal annealing*. Fig. 1 shows the resulting microstructure after heating to different target temperatures and holding at that temperature for 10^5s for the three homogenization variants considered in this work. For both C1-0 and C1-2 coarse elongated grain structures were observed after non-isothermal heating and annealing at 400 °C and 500°C, while recrystallization was mostly suppressed when annealing the same variants at the lower temperature of 300 °C. Statistical grain size measurements show that when increasing the target temperature from 400°C to 500°C, the average grain size increased from 163 to 184 µm, and from

160 to 203 µm for C1-0 and C1-2, respectively. On the other hand, C1-3 recrystallized completely also at 300°C, with a much refined grain structure as compared to the two former variants, and with only a slight increase in average grain size from 41 µm at 300 °C to 47 µm at 500 °C.
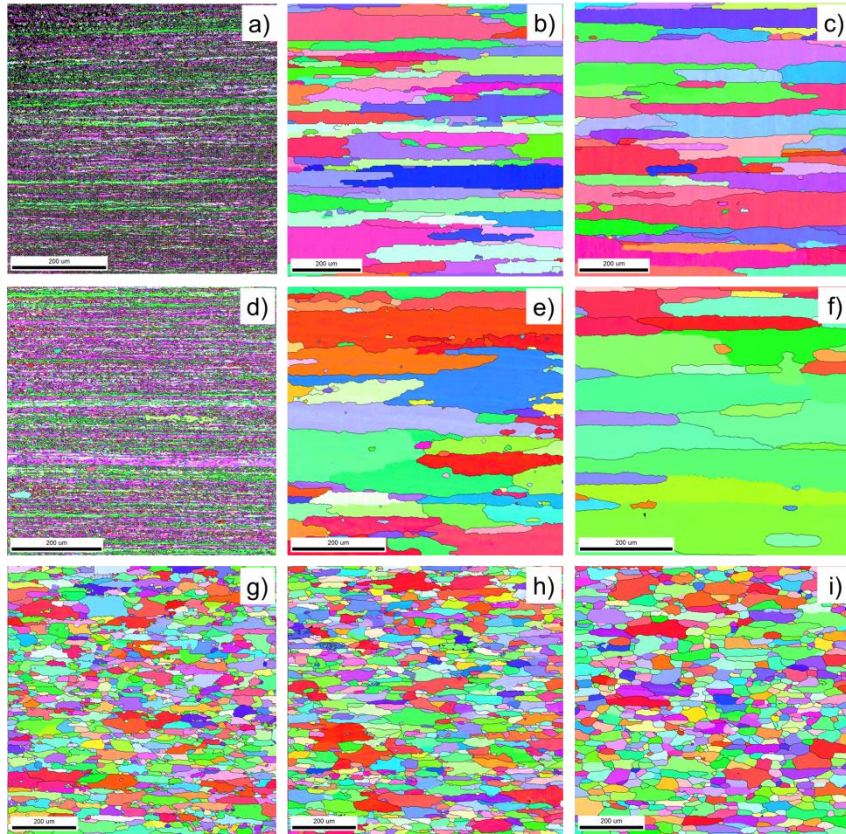

Fig. 1. EBSD micrographs showing the effect of microchemistry on the final recrystallized microstructure non-isothermally annealed to different temperatures and hold for 10^5s, samples were cold rolled to a strain of 3.0

a) C1-0, 300°C@10^5s; b) C1-0, 400°C@10^5s; c) C1-0, 500°C@10^5s

d) C1-2, 300°C@10^5s; e) C1-2, 400°C@10^5s; f) C1-2, 500°C@10^5s;

g) C1-3, 300°C@10^5s; h) C1-3, 400°C@10^5s; i) C1-3, 500°C@10^5s;

Also the texture is strongly affected by microchemistry after non-isothermal heating and annealing at different temperatures. Fig. 2 illustrates the textures in the form of the $\varphi_2 = 0°$ sections of the ODFs of the same conditions as presented in Fig. 1. Since recrystallization was mostly suppressed when annealing at 300°C for C1-0 and C1-2, a typical rolling texture component (i.e. Bs) is observed for these two cases, see Figs. 2a and 2d. The φ_1 of the scatter of the Bs component reaches to as high as 46.5° (cf. Fig. 2d) but still, overlap with the P component (φ_1=59.5°) is avoided since a reduced 10° scatter was applied in the definition of the latter (see above). From C1-0 to C1-3, corresponding to a significant decrease in the amount of Mn in solid solution, there is a clear transition in the recrystallization texture from a texture with a distinct high angle ND-rotated cube component ($\varphi_1 \approx$ 40°) to a texture with a true cube component ($\varphi_1 \approx$ 0°). For both C1-0 and C1-2 the dominant

recrystallization texture component is the P component, while the cube component is dominant in C1-3, as illustrated in Figs. 2g-h.
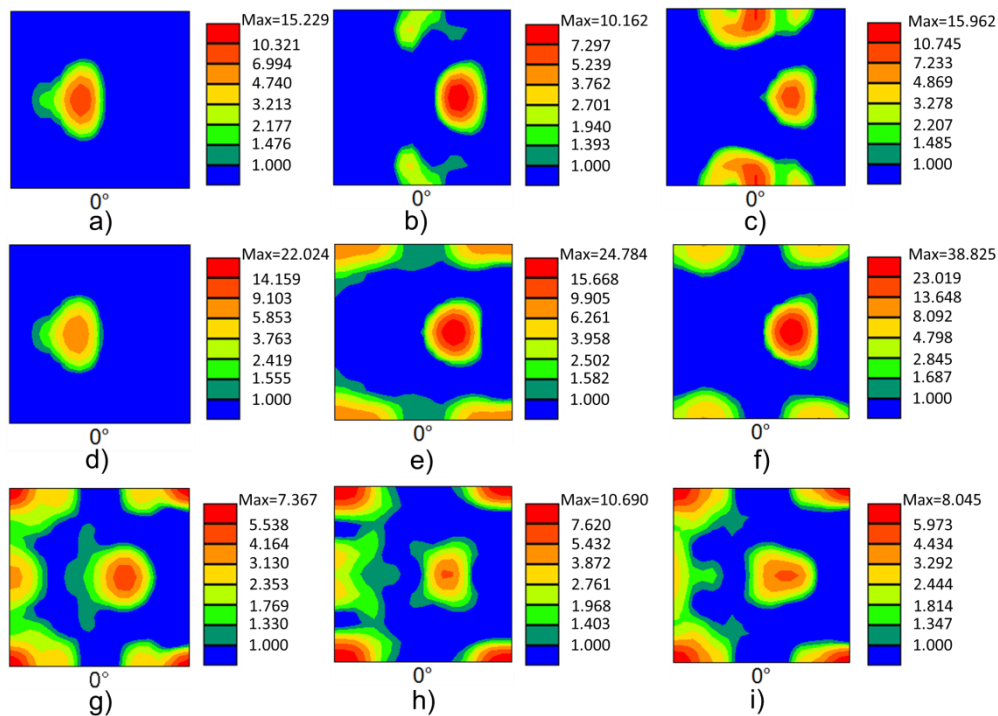

Fig. 2. ODF maps (φ_2=0) showing the effect of microchemistry on the final recrystallized microstructure non-isothermally annealed to different temperatures and hold for 10^5s, samples were cold rolled to a strain of 3.0

a) C1-0, 300°C@10^5s; b) C1-0, 400°C@10^5s; c) C1-0, 500°C@10^5s

d) C1-2, 300°C@10^5s; e) C1-2, 400°C@10^5s; f) C1-2, 500°C@10^5s;

g) C1-3, 300°C@10^5s; h) C1-3, 400°C@10^5s; i) C1-3, 500°C@10^5s;

The mechanical behaviour of the three variants, after non-isothermal heating to 400°C and keeping at temperature for 10^5 s, was analysed by tensile testing at room temperature; the stress-strain curves of the samples are shown in Fig. 3. The yield stresses were determined at 0.2% plastic strain ($R_{p0.2}$) and are compiled in Table 2, each yield stress being averaged from three tests conducted at the same conditions. Comparison of the different variants after the same annealing treatment shows that the flow stress of the as-cast variant C1-0 is appreciably larger than that of the other two variants C1-2 and C1-3, which both have very similar stress-strain behaviour. A more detailed analysis will be given in the discussion section.
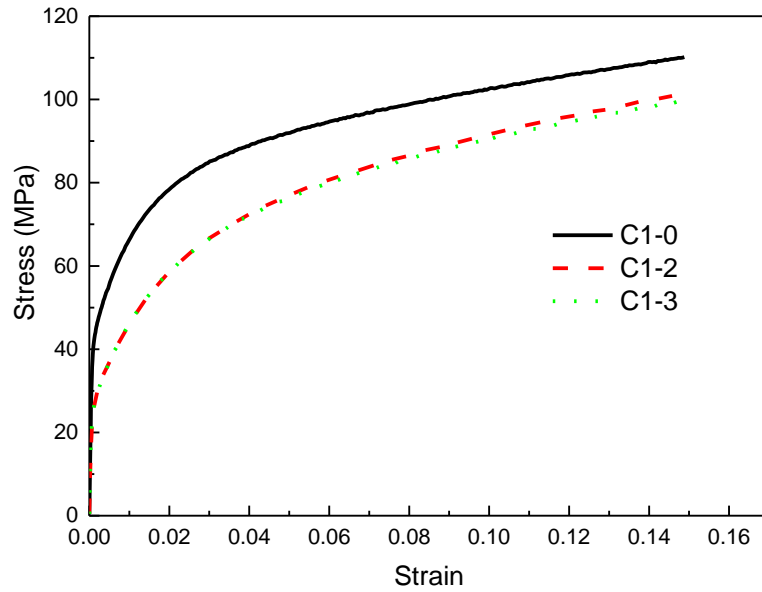
Fig.3. Stress-strain curves of the three variants non-isothermally heated to 400°C and then kept for 10^5s, samples were previously cold rolled to ε =3.0, tensile tests were performed at room temperature with strain rate of 10^{-3} s^{-1}

Table 2. Grain size, electrical conductivity and yield stress for the three variants, non-isothermally heated to 400°C and then kept for 10^5s, samples were previously cold rolled to ε =3.0

Condition	Grain size (µm)	Electrical conductivity (m/Ωmm^2)	Yield stress (MPa)
C1-0	163	31.3	49.4
C1-2	160	31.3	30.2
C1-3	44	30.7	30.8

## 3.3. Influence of microchemistry on microstructural evolution

As a basis to understand and possibly explain the differences in microstructure, texture and mechanical properties presented in Figs. 1-3, we now turn to a more detailed analysis of the non-isothermal heating stage. The evolution in hardness and electrical conductivity during heating up to 500 °C (without holding time) was monitored and is shown for all three variants in Fig. 4. Starting

8

with C1-0 variant, more than 50% of softening is obtained when the sample has reached to 350°C, while, as shown in Fig. 5a, only a few recrystallized grains where present, suggesting that recovery is the main reason for the significant softening which has taken place. At 400 °C, a fully recrystallized state has been reached, which is confirmed by EBSD analysis (cf. Fig. 5c). Fig. 4b reveals that the electrical conductivity increases considerably during heating, in particular in the temperature range from 300 to 350°C, suggesting significant concurrent precipitation during this period of heating. The hardness decreases for C1-2 until ~350°C where recrystallization is completed and it levels out with a further increase in temperature, as illustrated in Fig. 4a. For the electrical conductivity of C1-2, a notable increase is seen already when the material has reached to 200°C. At temperatures above 200°C the increase is accelerated, however, and a maximum is reached at about 400°C, comparably to what Liu *et al.* [22] observed in a similar material. The increase in electrical conductivity is due to concurrent precipitation from the solid solution, but it should be emphasized that the total increase in conductivity of only ~3 m/Ωmm^2 is considerably less than that of the C1-0 variant. It is noted that at maximum temperatures, when recrystallization is completed, a minor drop in the electrical conductivity is observed.

Finally we consider the evolution of Vickers hardness and electrical conductivity of C1-3 during non-isothermal annealing. Similar to that of C1-0 and C1-2, a slight increase in hardness was observed up to 200°C also in this case, the hardness then decreases rapidly and reaches to a stable value at ~325°C where recrystallization is completed, confirming the faster recrystallization kinetics than for C1-0 and C1-2. The electrical conductivity (Fig. 4b) for this variant increases first slowly (below 200°C), then more quickly before reaching to a maximum at about 350°C. It is noted however that the increase in conductivity is clearly less than that of C1-0 and C1-2 (Fig. 4b), which further illustrates that concurrent precipitation during non-isothermal annealing of C1-3 is less pronounced than for the two other variants.

a)

9
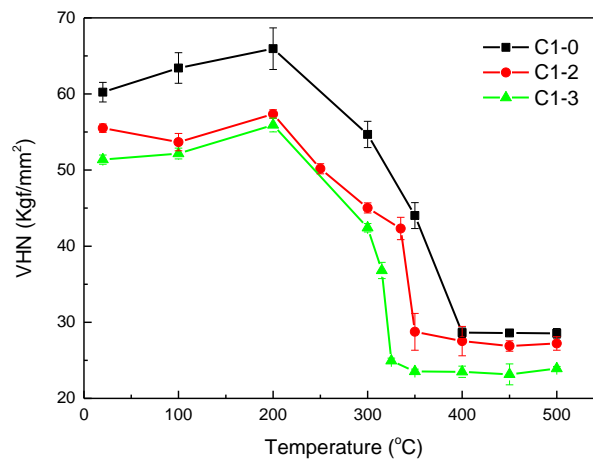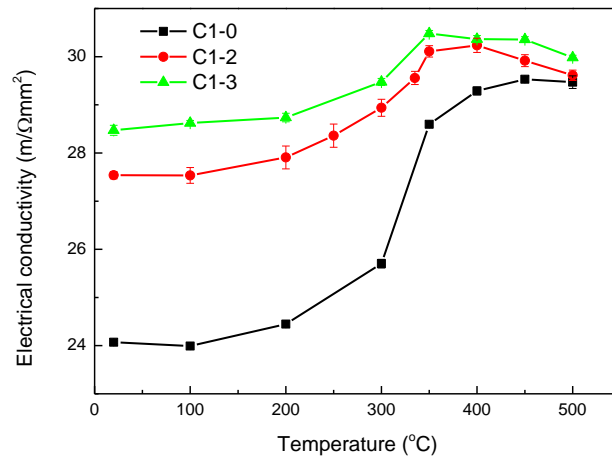
b)

Fig. 4. Hardness and electrical conductivity evolution of the three variants during non-isothermal heat treatment without holding time

a) Hardness; b) Electrical conductivity

The corresponding evolution in microstructure of the as-rolled sample C1-0 during continuous heating is shown in Fig. 5. Only a few recrystallized grains are visible after heating to 350°C, some of which are P-orientated (Fig. 5a). After further heating to 380 °C (Fig. 5b), a few recrystallized grains have grown significantly, preferentially along the RD direction. It is noted, however, that none of these are P-orientated grains, actually most of the recrystallized grains observed in Fig. 5b have the M orientation. A fully recrystallized state was obtained when the sample was heated to 400 °C (see Fig. 5c), where a large part of the grains are P or M orientated. It should be mentioned that there were many isolated islands within the coarse grains, apparently small grains surrounded by fast growing ones. Interestingly, according to Fig. 5c, the M and P-orientated grains do not seem to have any clear size advantage as compared to grains with other orientations.
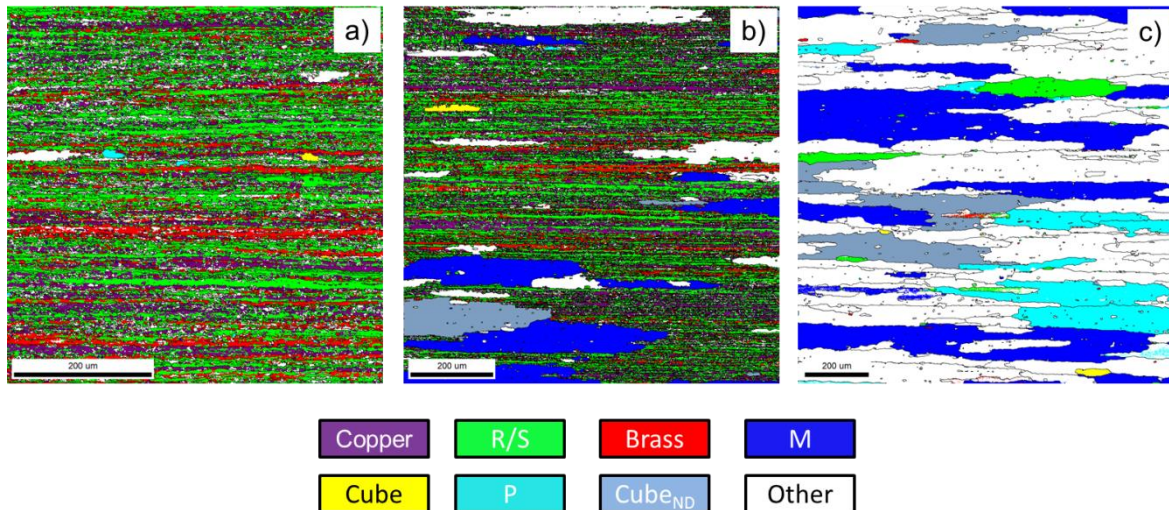
| Copper | R/S | Brass | M |
| Cube | P | Cube$_{ND}$ | Other |

Fig. 5. EBSD orientation micrographs showing the microstructure of C1-0 after non-isothermal heating experiments with samples cold rolled to 3.0. a) T=350°C,t=0s; b) T=380°C,t=0s; c) T=400°C,t=0s;

High magnification BSE images of the C1-0 material as heated to 350 °C are shown in Fig. 6. Obviously, a large number of fine dispersoids has already precipitated along grain/sub-grain boundaries, which are more or less aligned with the RD direction (see Fig. 6a and b). These precipitated dispersoids provide a significant drag effect along the ND direction, which is presumably responsible for the suppressed nucleation of recrystallized grains. The fact that precipitated dispersoids (as pointed out by the white arrows) retard the grain boundary migration is clearly visible in Fig. 6c, where only a certain segment of the grain boundary without any dispersoids is able to migrate undisturbedly, as indicated by the black arrow.
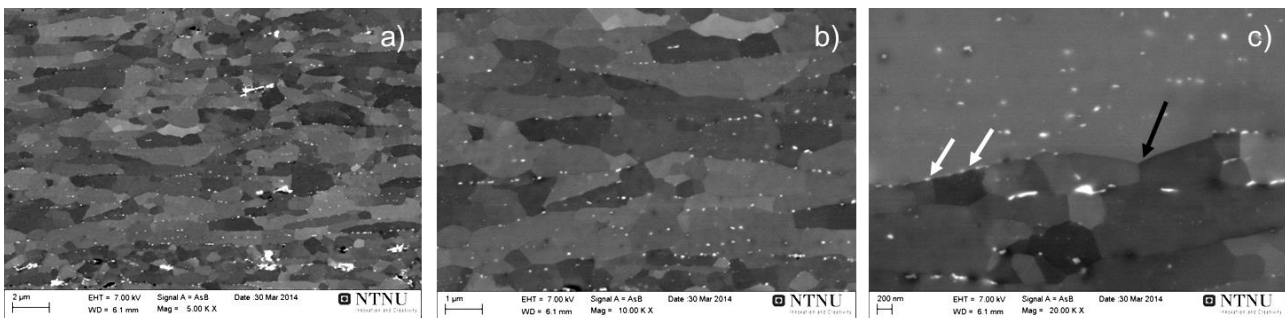

Fig. 6. BSE images showing the precipitated dispersoids of C1-0 after heating to 350°C

a) Overview of the second-phase particles

b) Dispersoids along the sub-grain boundaries; c) Dispersoids along the boundary of a growing recrystallized grain

Since the objective of the present work is to analyse how different microchemistry states influence the recrystallization behaviour during non-isothermal annealing we now turn to the C1-2 and C1-3 variants, for comparison. Starting with C1-2, it can be seen that some fairly large recrystallized grains with elongated shapes have already formed when the sample is heated to 325°C (Fig. 7a), though the number of recrystallized grains is very limited. Though the statistics is poor, it is worthy to notice

that none of these grains have a P or ND-rotated cube orientation which indicates that these orientations do not have any nucleation advantage. At 335°C, more recrystallized grains were observed, all of them were growing mainly along the rolling direction (Fig. 7b). At this stage the fractions of P and ND-rotated cube orientated grains are starting to dominate, and some of the P-orientated grains are obviously larger than grains with other orientations. Recrystallization is completed when the sample was heated to 350°C, and a pan-cake shaped grain structure is obtained, as shown in Fig. 7c.
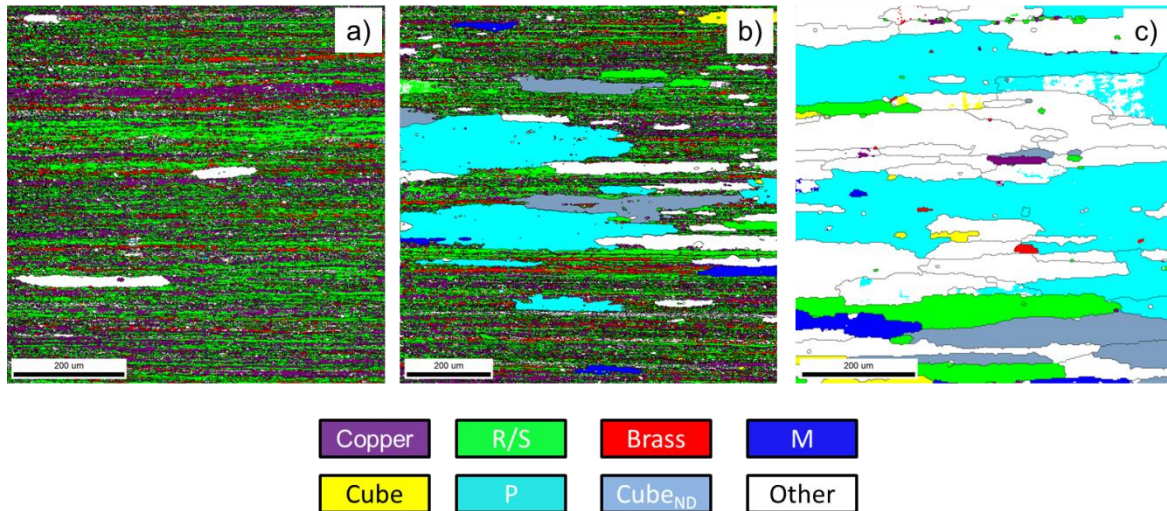

Fig. 7. EBSD map showing the microstructure of C1-2 after non-isothermal heating experiments with samples cold rolled to a strain of 3.0
a) T=325°C,t=0s; b) T=335°C,t=0s; c) T=350°C,t=0s;

The microstructure of sample C1-2 heated to 325°C was further analysed with BSE images as shown in Fig. 8. One recrystallized grain is present in Fig. 8a, whose growth in the ND direction seems to have stopped at high-angle grain boundaries which are aligned along RD direction. For this alloy less dispersoids are observed along the grain/sub-grain boundaries (Fig. 8b) as compared to the C1-0 variant, and some of them are actually located inside grains/sub-grains, examples are pointed out by the white arrows. Note however, that Fig. 6 and Fig. 8 refer to different temperatures which complicates a direct comparison; more dispersoids might be expected upon further heating to 350°C. Nonetheless, both pre-existing dispersoids and concurrently precipitated dispersoids are observed to pin the migration of the high-angle grain boundaries also for this alloy, as shown in Fig. 8c, where the larger particle indicated by the red arrow most likely is a pre-existing dispersoid. In general the pinning effect should be weaker than in C1-0.
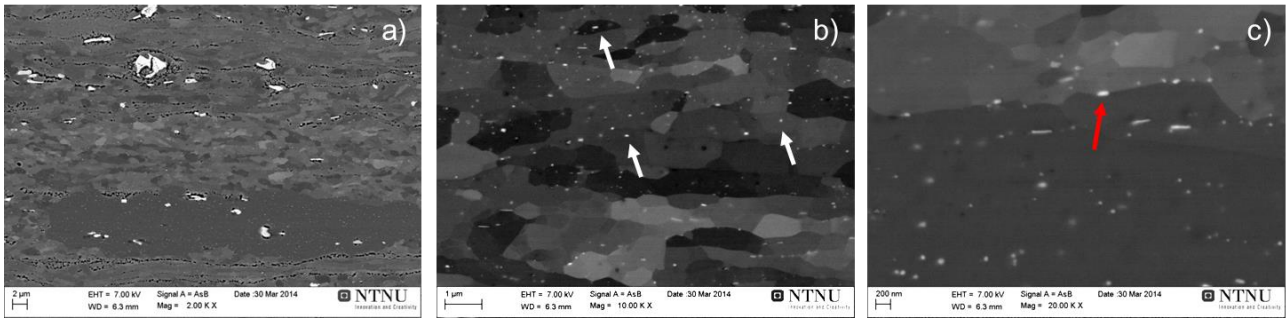
Fig. 8. BSE images showing the precipitated dispersoids of C1-2 after heating to 325ºC

a) Overview of the second-phase particles

b) Dispersoids along the sub-grain boundaries; c) Dispersoids along the boundary of a growing recrystallized grain

The corresponding microstructural evolution during non-isothermal annealing of C1-3 is illustrated in Fig. 9 and 10. It is observed from Fig. 9a that many recrystallized grains (with different orientations) are present already when the temperature has reached to 300°C, which contrasts both C1-0 and C1-2 where only a few recrystallized grains were visible at the early stage of recrystallization (Fig. 5a and Fig. 7a). The recrystallized grains present already at 300ºC grow larger with further heating to 315ºC (Fig. 9b) or 325ºC (Fig. 9c), the result of which is a refined grain structure with only slightly elongated grains. These recrystallized grains possess different orientations, where ~26% of the grains were S orientated, while only ~5% of the grains have P orientation. None of these grain orientations, however, seems to have a clear size advantage for the alloy C1-3, which has both limited concurrent precipitation and pre-existing dispersoids.
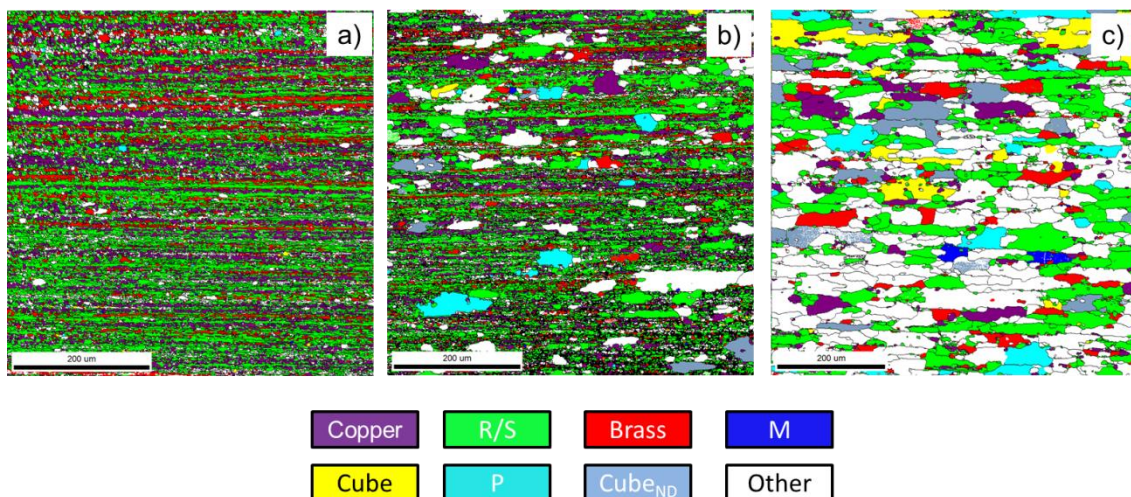

Fig. 9. EBSD map showing the microstructure of C1-3 after non-isothermal heating experiments with samples cold rolled to 3.0
a) T=300°C,t=0s; b) T=315°C,t=0s; c) T=325°C,t=0s;

For the C1-3 variant, recrystallization has clearly started already at 300°C which is the earliest for the three variants. A few recrystallized grains are visible in the BSE micrographs in Fig. 10a. As illustrated in Fig. 10b, both concurrent precipitation and pre-existing dispersoids are limited at this temperature. Indications of any concurrent precipitation is mainly at the early stage in the form of tiny white solute enriched zones, i.e. Mn, Si (and Fe), as indicated by the white arrows in Fig. 10b. The pre-existing dispersoids in C1-3 are obviously larger but lower in density than in the variant C1-2. Still, just as for C1-2, both assumedly concurrently formed precipitates and pre-existing dispersoids are observed to pin the migration of high angle grain boundaries. An example for this is shown in Fig. 10c, where the larger particle indicated by the black arrow is most likely a pre-existing dispersoid.
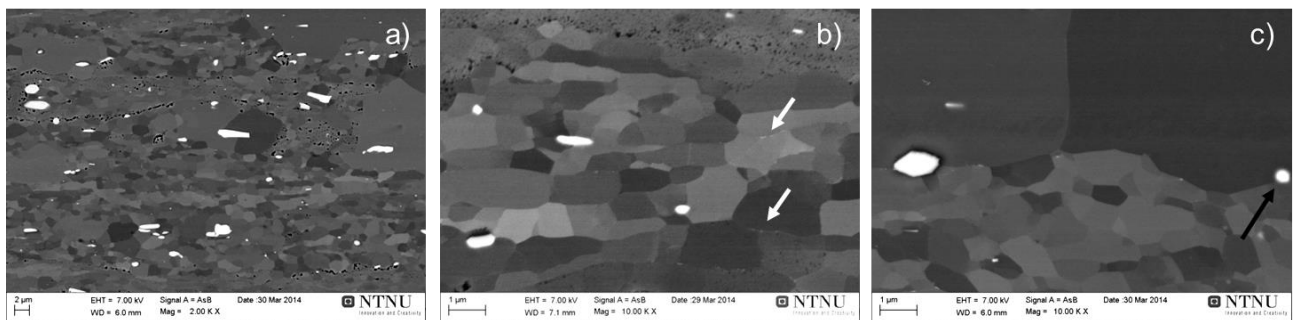

Fig. 10. BSE images showing the precipitated dispersoids of C1-3 after heating to 300°C

a) Overview of the second-phase particles

b) Dispersoids along the sub-grain boundaries; c) Dispersoids along the boundary of a growing recrystallized grain

The SEM BSE images shown in Figs. 6, 8 and 10 are associated with different temperatures, which make a direct comparison of the concurrent precipitation behaviour difficult since it is also temperature dependent. Therefore, SEM BSE images of the dispersoid structures for the three variants were also obtained for a constant temperature of 300°C, see Fig. 11. When heating to 300°C from room temperature, the increment in electrical conductivity (see Fig.4b) is 1.7, 1.1 and 1.0 $m/\Omega mm^2$ for C1-0, C1-2 and C1-3, respectively. This is in line with the observation shown in Fig. 11 where C1-0 (Fig. 11a) clearly has the strongest concurrent precipitation and C1-3 has the weakest (Fig. 11c). After heating to 300°C, concurrently precipitated dispersoids are mixed with pre-existing ones for C1-2, which makes it difficult to distinguish between the two (Fig. 11b). However, quantitative measurements shows that the total dispersoid number density in this condition is $\sim 4.0 \times 10^6$ mm^{-2}, i.e. much larger than the number density of the pre-existing dispersoids (1.3×10^6 mm^{-2}; cf. Table 1). This confirms that C1-2 has experienced significant additional precipitation during continuous heating from ambient temperature to 300°C. Thus, during non-isothermal heating to higher temperatures, precipitation starts already at low temperatures, and a strong influence both on recovery and recrystallization is inevitable.
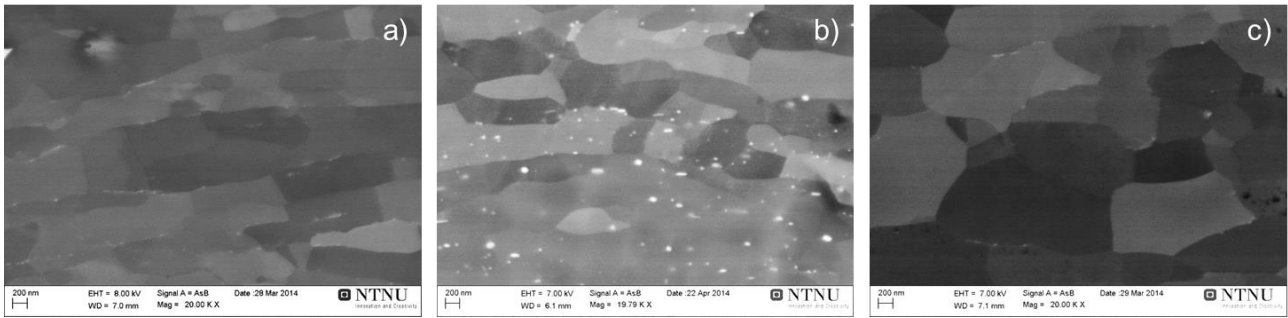
Fig. 11. BSE images showing the precipitated dispersoids of the three variants after heating to 300ºC

a) C1-0; b) C1-2; c) C1-3

3.4. Influence of microchemistry on recrystallization texture

From Figs. 1 and 2 and Figs 5, 7 and 9, it is clearly documented that different microchemistry states lead to different grain structures and textures. However, to get statistically more reliable texture data – especially for the coarse grained materials – a large area was scanned for each of the three variants. The results are shown in Fig. 12 in the form of full ODFs. The recrystallization texture of the C1-0 variant is characterized by strong P (~10x random) and {113}<110> M texture components (indicated by the red arrow, ~ 6x random), where also some weak ND-rotated cube (~3x random) was present, see Fig. 12a. The occurrence of the M orientation was also reported during annealing of a deformed supersaturated Al-Mn alloy AA3003 [26]. As illustrated in Fig. 12b, an extremely sharp P texture (~33x random) was obtained for the C1-2 variant together with a relatively weaker ND-rotated cube texture component. Sharp P and ND-rotated cube texture components have also been observed during isothermal annealing with concurrent precipitation [17,18]. It has also been observed that the intensities of these components can become significant after isothermal annealing of commercially pure AA1050 alloy deformed to ultrahigh strains [33]. It is well documented that large deformation strains, high supersaturation levels of Mn and low annealing temperature promote the P texture [7,17,26]. As apparent from Fig. 12c, for the C1-3 variant a relatively weaker texture was observed, dominated by both cube (~ 7x random) and P texture components (~5x random). For the Al-Mg alloy AA5182 [20] it has been found that recovery of cold-rolled sheets prior to recrystallization annealing promoted the formation of {124}<211> R texture, but restrained the formation of the cube texture. Recovery does take place during heating before the onset of recrystallization in the present study, however, the R texture was absent for both C1-0 and C1-2 (Fig. 12a, b), while a weak R texture was obtained for C1-3 (Fig. 12c).
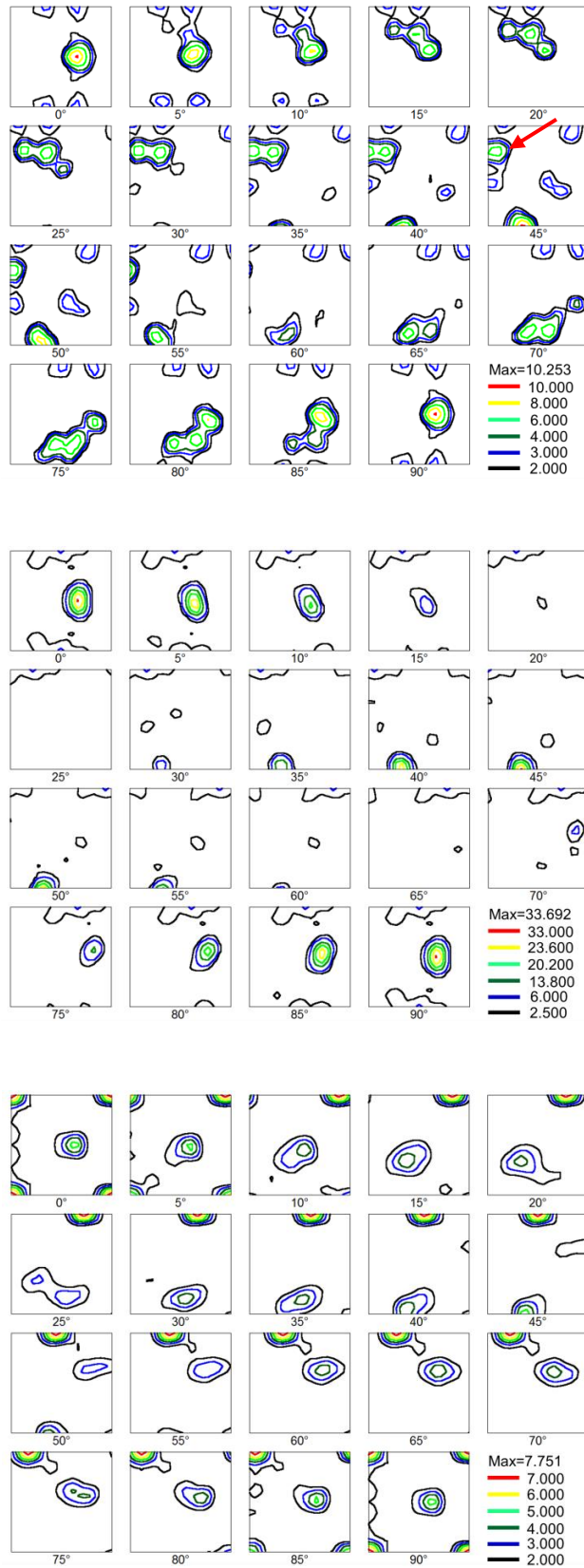
Fig. 12. Recrystallization texture of the three variants

a)   C1-0, 400 ℃, t=0s, b) C1-2, 350 ℃, t=0s, c) C1-3, 325 ℃, t=0s,

16

3.5. Origin of the P texture component

It has been demonstrated experimentally by EBSD [18,24,34,35] and TEM [32,36] that P-orientated grains/sub-grains are present already within the deformation zone around constituent particles after deformation. This fact has further been confirmed by numerical simulations of the texture evolution within the deformation zone of second-phase particles [37,38]. In the present study, P-orientated grains indeed can be found near constituent particles after deformation, which are shown as non-indexed black areas in the EBSD maps. An example is highlighted by the black arrow in Fig. 13a which shows the C1-2 alloy in the as-deformed state (strain of $\varepsilon = 3.0$). This was also seen after heating to 325°C, see Fig. 13b, for which the quality of the EBSD maps is much better, though recovery is still the dominating softening mechanism (cf. Fig. 4a) and only small number of recrystallized grains can be found (cf. Fig. 7a). In the high-resolution scan presented in Fig. 13b small equiaxed P-orientated grains can again be observed near particles. However, a few elongated P-orientated grains, with clear sub-grain boundaries inside, are also observed far away from large particles (although the possibility that particles lie beneath the polished surface cannot be ignored), as shown in Fig. 13c. This latter observation indicates that some of the P-orientated grains may also originate from the deformed matrix, and not solely from the deformation zones around large particles.
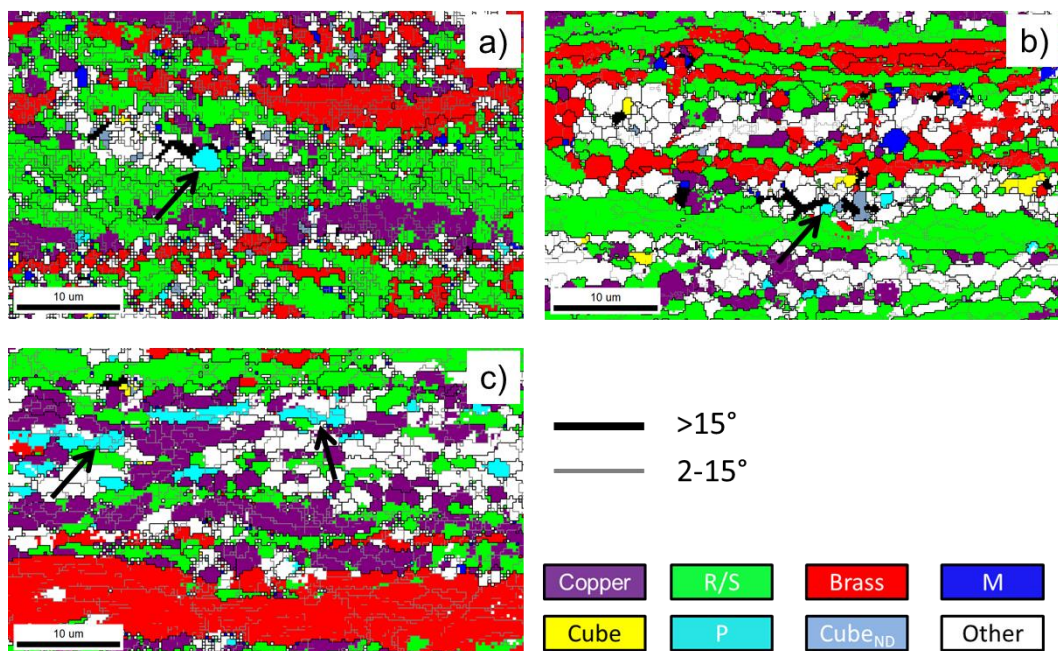

Fig. 13. Detailed analyses on the formation and development of P-orientated grains. EBSD orientation maps are scanned with step size from 0.2-0.3µm, and non-indexed points are displayed in black, the black lines represent high angle grain boundaries with θ > 15°, grey lines represent low angle grain boundaries with 2<θ<15°: a) Deformed sample of C1-2, with ε=3.0; b) Deformed sample of C1-2 (ε=3.0), heated at 50 K/h to 325°C, showing the P-orientated grains near particles; c) The same condition as b) showing the elongated P-grains, with visible misorientation inside.

17

4. Discussion

The experimental results have revealed good evidence that different homogenization procedures of an as-cast Al-Mn-Fe-Si model alloy gave rise to characteristic differences in microchemistry state, i.e. solute Mn and Mn-containing dispersoids. After cold rolling and non-isothermal annealing these microchemistry differences led to distinctively different recrystallization kinetics, grain structure and texture as well as mechanical properties. In what follows these differences are explained based on the effect of concurrent precipitation and pre-existing dispersoids.

4.1. Concurrent precipitation

It is well known that dispersoids may greatly affect recrystallization kinetics as well as the evolution of microstructure and texture upon annealing of deformed metallic materials (e.g. [5-8]). Alloy variants with a large fraction of small dispersoids will experience large back-driving force and, hence, slow recrystallization kinetics (cf. Fig. 4a). The opposite effects of size, r, and volume fraction, f, of the dispersoids are commonly incorporated in the Zener drag p_Z, which provides a back-driving, or retarding, pressure on the moving high-angle grain boundaries upon progressing recrystallization:

$$p_Z = \frac{3}{2} \cdot \gamma_{GB} \cdot \frac{f}{r} \tag{1}$$

where γ_{GB} is the specific grain boundary energy.

For the as-cast variant C1-0, which contains the highest level of Mn in solid solution, strongest concurrent precipitation was observed, which is consistent with the largest increase in electrical conductivity experienced by this variant (>5 m/Ωmm^2, see Fig. 4b) during annealing and with the highest flow stress after recrystallization (Fig. 3). The precipitated dispersoids were located mostly along high angle and sub-grain boundaries (see Fig. 6a) and the migration of grain boundaries was strongly retarded, and this variant thus yielded the slowest recrystallization kinetics. In contrast, C1-2 has a large amount of pre-existing dispersoids and a lower level of Mn in solid solution prior to annealing. The somewhat faster recrystallization kinetics of C1-2 in comparison to C1-0 indicates that pre-existing dispersoids have a less profound effect on retarding recrystallization. This is probably because pre-existing dispersoids are coarser than particles forming concurrently with recrystallization. Moreover, pre-existing dispersoids are presumably more randomly distributed (cf. Fig. 8), some of them located inside sub-grains, providing a less effective Zener drag than those formed concurrently [18]. It should be noted though that pre-existing dispersoids are also observed to pin the migration of grain boundaries, as exemplified in Fig. 8c and Fig. 10c. On the other hand, dispersoids formed by concurrent precipitation, which are mostly found along grain/sub-grain boundaries (Fig. 6b), more effectively suppress nucleation (by pinning sub-grain boundaries) and prevent or retard the migration of the moving front of the recrystallized grain boundaries [7].

The lack of differences in flow stress behaviour for the two variants C1-2 and C1-3 (see Fig. 3) was already analysed in Ref. [23], taking into account the effects from grain size, texture, as well as solid solution. It is well known that the yield stress generally depends on the grain size and the grain size contribution can be estimated through the Hall-Patch relation $\sigma = \sigma_0 + kd^{-1/2}$, using $k = 0.78$

MPa·mm$^{1/2}$ for 99.5% commercially pure aluminium [39]. A decrease of the grain size from ~160 µm to ~40 µm only gives an increase of the yield stress of ~2 MPa. That is why, as compared to the other two variants with coarser grain sizes, the flow stress of C1-3 does not increase significantly. The much higher flow stress for the C1-0 variant is mainly attributed to dispersion hardening due to the large density of small particles forming through concurrent precipitation [40, 41]. Even though the electrical conductivities of C1-0 and C1-2 are quite similar after non-isothermal annealing at 400°C for 10^5s (see Table 2), it should be noted that the initial electrical conductivities (see Table 1) of these two variants are quite different. Since C1-0 has a much lower initial conductivity than C1-2, more concurrent precipitation have taken place for this variant such that it exhibits similar electrical conductivity as C1-2 after annealing. Evidence for the strong concurrent precipitation in C1-0 is provided by the large significant in electrical conductivity of 7.4 m/Ωmm^2 (see Table 1 and Table 2), as well as direct observation of a large amount of dispersoids shown in Fig. 6. Muggerud *et al.* [41] estimated the contribution of dispersoids to yield strength from TEM measurements to be ~24 MPa when annealing the as-cast variant (without deformation) at 50 K/h to 375°C and keeping for 24h. In the current study, the flow stress of C1-0 is 18.6 MPa higher than that of C1-3 (see Table 2), which is slightly lower than the contribution from dispersoids calculated in Ref. **Error! Bookmark not defined.**[41]. The fact that C1-3 also contains some dispersoids and its recrystallized grain size is much smaller (Table 2), together with the higher annealing temperature (400°C in the current study) may all be responsible for the somewhat smaller difference in flow stress between C1-0 and C1-3.

In terms of hardness evolution during non-isothermal annealing, it should be noted that before reaching to 200°C all three variants showed a slight increase in hardness (see Fig. 4a). This phenomenon which is referred to as "hardening upon annealing" is usually associated with nanostructured materials during low temperature annealing [42]. However, the same phenomenon has also been observed during isothermal annealing at low temperatures after heavy deformation of similar alloys as those considered in this work [14, 43, 44]. Even though the exact mechanisms causing hardening on annealing are not clarified yet, it has been argued that some sort of clustering or precipitation mechanism is involved [44].

At temperatures above 350°C, a drop of electrical conductivity is observed for C1-2 and C1-3 (see Fig. 4b). This drop may be due to the fact that at these temperatures, dispersoids will re-dissolve back into the matrix due to the increased solubility of Mn in the matrix at higher temperatures [12]. A similar evolution of electrical conductivity was observed by Li *et al.* [12,13] using a *non-deformed* as-cast AA3003 alloy, where the electrical conductivity likewise developed a maximum, though at a higher temperature of 530°C. These observations indicate that precipitation of dispersoids in the present as-deformed material is faster and finer than in the as-cast state, which is due to a higher diffusion rate of alloying elements and more heterogeneous nucleation sites for precipitation of dispersoids for the former case.

4.2. Impact of concurrent precipitation on microstructural evolution

The present study substantiates that differences in microchemistry may strongly influence the evolution of grain structure during non-isothermal annealing. Qualitatively, strong concurrent precipitation (as in variant C1-0) or a large number of pre-existing dispersoids (in C1-2) both favour the formation of coarse elongated recrystallized grains. Vice versa, a much finer equiaxed grain structure can be obtained when both concurrent precipitation and pre-existing dispersoids are limited (C1-3). As can be seen from Table 2, the average recrystallized grain sizes of C1-0, C1-2 and C1-3 are 163 µm, 160 µm and 44 µm, respectively. These data are consistent with the conclusions of Tangen *et al.* [18] that dispersoids present prior to cold rolling and annealing have a weaker effect on the recrystallized grain size compared to those forming through concurrent precipitation during *isothermal annealing* of Al-Mn alloys. Also for the C1-3 variant the growing grains during continuous heating suffer a Zener drag in the ND direction due to dispersoids precipitated along old grain boundaries aligned with the RD direction (see Fig. 9). However, this Zener drag is significantly lower for C1-3 than that of the other two cases, due to coarser pre-existing dispersoids as well as a smaller potential for concurrent precipitation, see Figs. 4 and 10.

During non-isothermal annealing considerable precipitation of dispersoids may take place at low temperatures before the onset of recrystallization (see Fig. 6b). Thus, these dispersoids will act as "pre-existing dispersoids" in the sense that recrystallization is not yet initiated. However, one important difference as compared to true pre-existing dispersoids is that the size of most of the concurrently precipitated dispersoids are smaller than the pre-existing ones, and they are mostly located at grain/sub-grain boundaries, which are aligned with the RD direction. It has been shown by the SEM BSE micrographs that the elongated grain structure can mainly be ascribed to the concurrently precipitated dispersoids, but the pre-existing ones also play a role. Further investigations focusing on differentiating the contribution from pre-existing dispersoids and concurrent precipitation on the recrystallization behaviour is currently underway. During non-isothermal annealing, recovery occurring during the slow heating below the onset of recrystallization will reduce the stored energy and thus the driving force for nucleation of recrystallization. This is also one of the reasons for the final grain size of the three variants after complete recrystallization being much larger than those obtained after isothermal annealing at 300-500°C [14].

Prior and concurrent precipitation also significantly delays the onset of recrystallization during non-isothermal annealing, see Fig.4a. The temperature at which recrystallization starts thus decreases in turn from C1-0 to C1-3, as illustrated in Fig.5, Fig.7 and Fig.9. This is closely connected to the initial microchemistries of these three variants (see Table 1) where the concentration levels of Mn in solid solution decrease from C1-0 to C1-3. C1-0 has the highest initial concentration level of Mn in solid solution, and the strongest (concurrent) precipitation is thus observed for this variant, as evidenced by Fig.6, Fig.8, Fig.10 and Fig.11. Strong (prior and concurrent) precipitation suppresses nucleation and increases the temperature for the onset of recrystallization. That is why the recrystallization started at 350°C, 325°C and 300°C for C1-0, C1-2 and C1-3, respectively.

4.3. Impact of concurrent precipitation on texture

In terms of recrystallization texture, one of the most striking results of the present study is the very sharp P texture that was obtained for the variant C1-2 after non-isothermal annealing. As already mentioned earlier, the P texture component has repeatedly been observed to prevail in materials with

strong Mn-supersaturation which were either annealed at low temperatures or non-isothermally with low heating rates, i.e. in instances when precipitation of dispersoids occurs prior to or concurrently with recrystallization [7,17,18,26]. Tangen *et al.* [18] investigated the recrystallization behaviour of a cold-rolled Al-Mn alloy and reported that, in the case of concurrent precipitation, grains with P and ND rotated cube orientation have an initial growth advantage compared to grains with other orientations. They suggested that the reason for the P and ND rotated cube-orientated grains to grow faster than other grains is due to their approximate 38° <111> orientation relationship ($\sum$7-type CSL grain boundary) with the neighbouring Cu deformation texture component. The reason is that the special boundaries of this kind are more ordered and have a lower specific grain boundary energy – up to ~10% lower than those of regular high-angle grain boundaries [45]. In more recent investigations, even larger differences in the energies between $\sum$7 and regular high angle grain boundaries have been reported in Al films [46] and polycrystalline nickel [1], respectively. Such special boundaries are less affected by concurrent precipitation and solute drag effects, firstly because the highly ordered structure yields less potential for nucleation of dispersoids, and secondly since the reduced grain boundary energy γ_{GB} leads to a lower Zener drag (Eq. (1)). Similar effects have also been reported for particle-containing copper single crystals [45], Fe-Cr alloys [48] and Fe-Si transformer steel [49].

In order to elucidate the relevance of special $\sum$7 grain boundaries in explaining the dominance of the P texture, the probability of $\sum$7 boundaries was estimated for the rolling texture of the present material. For that purpose, 5000 orientations (with a high confidence index) were taken at random from the EBSD data set of the as-deformed structure of sample C1-3. Each of these orientations representing the material's rolling texture was numerically rotated by 38.2° about the 8 possible <111> axes; the resulting 40,000 orientations are represented in Fig. 14 in the form of an ODF of the so-called transformation texture. It appears that both P and ND rotated cube-orientations reveal rather strong intensities in the transformation texture, which implies that these orientations will indeed have larger fractions of $\sum$7 grain boundaries than grains with other orientations. Note that the M orientation which is also found in samples with pronounced concurrent precipitation is likewise observed in the transformation texture.
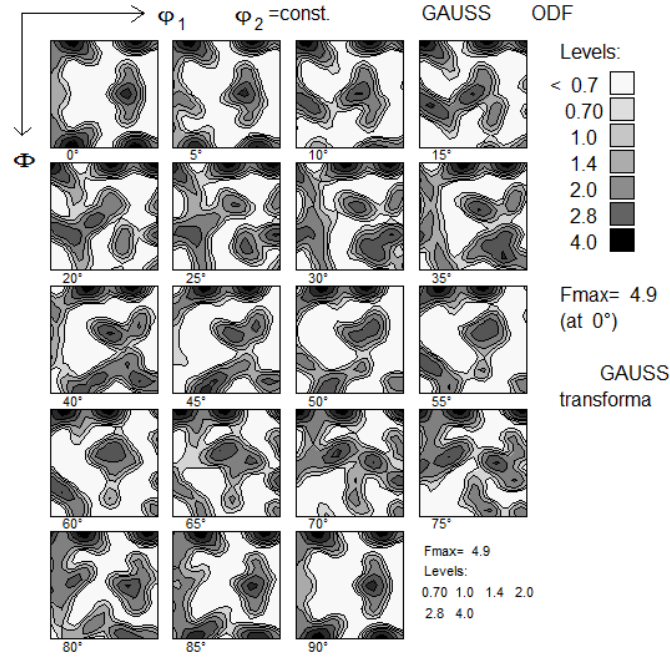
21

Fig. 14. Transformation of the rolling texture by 38.2° <111>, corresponding to special ∑7 CSL grain boundaries.

In their study on the influence of concurrent precipitation during *isothermal annealing*, Tangen *et al.* [18] obtained an increased intensity of the P texture component when increasing the initial supersaturation of Mn. In the present work with non-isothermal heating, the same tendency is not observed, however. The intensity of the P texture component is actually lower for the as-cast variant (C1-0) than for C1-2, though C1-0 has the highest initial supersaturation of Mn and thus the highest potential for concurrent precipitation. The sharp P texture of the present C1-2 variant can neither just be explained by a large number of pre-existing dispersoids or orientation pinning during recrystallization [33], since the P component was observed to be fairly weak during isothermal annealing of the same alloy [14]. The strength of the P texture has been found to increase with the amount of deformation before annealing of AA3xxx alloys [17, 18, 50], especially upon hot deformation [50]. The same tendency was found even for commercial purity AA1050 cold-rolled to ultrahigh strains [33], but the effect of strain is clearly not the reason of the particular sharp P texture for C1-2 since the same cold deformation was applied to the three variants.

The lower onset temperature for recrystallization may have contributed to the sharp P texture of C1-2 variant after recrystallization. It is well documented that increasing the annealing temperature will decrease the intensity of the P texture component [17, 26]. Recrystallization in the C1-2 sample started when it was heated to 325°C during non-isothermal annealing, while for the as-cast variant (C1-0), recrystallization initiated first at ~350°C. As already stated earlier, grain boundary migration of recrystallized grains is influenced by pre-existing dispersoids as well as concurrent precipitation (Figs. 8c and 10c). However, while all of the pre-existing dispersoids will have an influence on retarding grain boundary migration, only a part of them (mainly those along grain/sub-grain boundaries) will influence the nucleation of recrystallization. The fact that the P-orientated grains are not obviously larger than other grains during non-isothermal annealing of C1-0 (which has the

22

strongest concurrent precipitation) may indicate that the growth advantage period of the P-oriented grains in these alloys is in a temperature regime lower than 350°C. The latter is also consistent with the recrystallization behaviour of the C1-2 variant where some very large P-oriented grains are observed just after onset of recrystallization in this alloy, around ~335ºC (Fig. 7b). This growth advantage at low temperature is obviously also related to the amount of concurrent precipitation, since a weaker P texture was obtained for the C1-3 variant where recrystallization took place at an even lower temperature and concurrent precipitation was limited.

It is noted that a dominant P-texture (sometimes complemented by the ND-rotated cube component) is generally accompanied by a coarse-grained microstructure. This means that the absolute number of P-oriented nuclei is very low and the P-texture becomes dominant only when all other nucleation and oriented growth mechanisms are strongly suppressed. For example, the C1-3 alloy has a similar deformation texture and, in consequence, also a 38.2º <111> transformation texture similar to C1-2 (Fig. 14). Nevertheless, during recrystallization of C1-3 other nucleation and growth mechanisms outweigh the P-oriented grains and the P-texture becomes much less dominant.

Another interesting feature is the appearance of the M texture for the C1-0 variant. The M texture component was first reported in AA3xxx series aluminium alloys by Liu and Morris [26], where a strong M texture was observed during isothermal annealing of a supersaturated Al-1.0 wt.% Mn alloy at low temperatures. The intensity of the M texture component was higher than that of P component when annealing at temperatures below 400°C. Since it is not really a well-recognized recrystallization texture orientation, this component is often overlooked [14, 18] when only parts of the ODFs (e.g. $\varphi_2 = 0\,°$ sections) are analysed. In the present study, with only 0.39 wt.% of Mn, the strength of the M component was lower than that of the P component even for the as-cast variant C1-0, which has the highest potential for concurrent precipitation. The intensity of the M texture component is clearly dependent on the solute level of Mn, with only a small number of M-orientated grains being present after full recrystallization for the C1-2 and C1-3 samples as shown in Figs. 7c and 9c, respectively (for further evidence see also Fig. 12b and Fig. 12c). It should also be pointed out that the temperatures at which M-orientated grains are observed are also dependent on the microchemistry state, with this temperature increasing with the solute level of Mn in the alloys. As an example, few M-orientated grains were already present when annealing variant C1-2 to 325°C, while no M-orientated grains were observed in C1-0 until heating up to 380°C.

5. Conclusions and outlook

Microchemistry has previously been found to have a significant effect on the recrystallization grain structure and texture after isothermal annealing of Al-Mn-Fe-Si alloys [14, 18, 19]. In the present paper, the gradual microstructural and texture evolution during *non-isothermal annealing* has been investigated in detail by SEM/EBSD. The following conclusions can be drawn.

(1) Microchemistry strongly affects recrystallization kinetics, with high levels of Mn in solid solution giving slow recrystallization during annealing of cold-rolled Al-Mn-Fe-Si alloys because of suppressed recrystallization nucleation due to concurrent precipitation. The degree of concurrent precipitation increases with increasing initial supersaturation level of Mn in solid solution.

(2) Concurrently precipitated dispersoids are mostly located along grain/sub-grain boundaries. Both concurrent precipitation and pre-existing dispersoids retard grain/sub-grain migration, but the latter one has a less significant effect on retarding recrystallization kinetics than the former.

(3) Strong prior (during annealing) and concurrent precipitation suppresses nucleation and increases the temperature for the onset of recrystallization, which finally leads to a coarse and pan-cake shaped grain structure, accompanied by strong P {011}<566> and/or M {113}<110> texture components together with a relatively weaker ND-rotated cube {001}<310> component.

(4) A fine equiaxed grain structure with medium strength P and Cube {001}<100> texture components was obtained when the pre-existing dispersoids were coarser and fewer while concurrent precipitation was limited.

(5) The microchemistry state also affect the mechanical properties of the recrystallized condition, mainly in terms of a dispersion hardening effect where a high density of fine dispersoids changes the stress-strain behaviour and gives a significantly higher yield stress.

(6) It is shown that nucleation and growth of grains with different orientations are highly temperature and microchemistry dependent. Some of the P-orientated grains are less affected by dispersoids and experience a growth advantage at low temperatures, while M orientated grains prevail at relatively higher temperatures. The intensity of the P texture, however, does not increase with the supersaturation level of Mn as observed during isothermal annealing, as opposed to the M texture component where the supersaturation level of Mn seems to promote its presence.

The results shown in this paper substantiate that the microchemistry state, in terms of the solute level of Mn, size and spatial distribution of the second-phase particles, as well as their temporal evolution, need to be accounted for in detail in order to get an accurate prediction of the softening behaviour and the final grain structure and texture. Thus, numerical models [e.g. 21, 38, 52] which take into account the interaction between recrystallization and second-phase particles will be helpful to obtain a better understanding of this complicated interaction.

References

[1] F.J. Humphreys, Acta Metall. 25 (1977) 1323–1344.

[2] R.D. Doherty, D.A. Hughes, F.J. Humphreys, J.J. Jonas, D. Juul Jensen, M.E. Kassner et al., Mater. Sci. Eng. A 238 (1997) 219–274.

[3] F.J. Humphreys, Acta Mater. 45 (1997) 4231–4240.

[4] F.J. Humphreys, Scripta Mater. 43 (2000) 591–596.

[5] O. Daaland, E. Nes, Acta Mater. 44 (1996) 1413–1435.

[6] E. Nes, N. Ryum, O. Hunderi, Acta Metall. 33 (1985) 11-22

[7] F.J. Humphreys, M. Hatherly, Recrystallization and Related Annealing Phenomena, second ed., Elsevier, Oxford, 2004.

[8] A.R. Eivani, S. Valipour, H. Ahmed, J. Zhou, J. Duszczyk, Metall. Mater. Trans. 42A (2011) 1109-1116

[9] F.J. Humphreys, P.N. Kalu, Acta Metall. Mater. 35 (1987) 2815-2829

[10] Y.J. Li, W.Z. Zhang, K. Marthinsen, Acta Mater. 60 (2012) 5963-5974

[11] Y.J. Li, A.M.F. Muggerud, A. Olsen, Acta Mater. 60 (2012) 1004-1014

[12] Y.J. Li, L. Arnberg, Acta Mater. 51 (2003) 3415–3428

[13] Y.J. Li, L. Arnberg, Mater. Sci. Eng. A 347 (2003) 130-135

[14] K. Huang, N. Wang, Y.J. Li, K. Marthinsen, Mater. Sci. Eng. A 601 (2014) 86-96

[15] M. Somerday, F.J. Humphreys, Mater. Sci. Technol. 19 (2003) 20-29

[16] W.C. Liu, J.G. Morris, Metall. Mater. Trans. 36A (2005) 2829-2848

[17] H.E. Vatne, O. Engler, E. Nes, Mater. Sci. Technol. 13 (1997) 93-102

[18] S. Tangen, K. Sjølstad, T. Furu, E. Nes, Metall. Mater. Trans. 41A (2010) 2970-2983

[19] K. Huang, Y.J. Li, K. Marthinsen, Trans. Nonferr. Met. Soc. China 24 (2014) 3840-3847

[20] W.C. Liu, J. Li, H. Yuan, Q.X .Yang, Scripta Mater. 57 (2007) 833-836

[21] C. Schäfer, V. Mohles, G. Gottstein, Acta Mater. 59 (2011) 6574-6587

[22] W.C. Liu, Z. Li, C.S. Man, Mater. Sci. Eng. A 478 (2008) 173-180

[23] K. Huang, Y.J. Li, K. Marthinsen, J. Mater. Process. Technol (Submitted)

[24] C. Schäfer, G. Gottstein, Int. J. Mater. Res. 102 (2011) 1106-1114.

[25] C.C. Bampton, J.A. Wert, M.W. Mahoney, Mater. Trans. 13A (1982) 193-198

[26] W.C. Liu, J.G. Morris, Scripta Mater. 56 (2007) 217-220

[27] K. Huang, Y.J. Li, K. Marthinsen, Mater. Sci. Forum 783-786 (2014) 174-179

[28] K. Huang, Y.J. Li, K. Marthinsen, Mater. Sci. Forum 794-796 (2014) 1163-1168

[29] Y.H. Zhang, D. Juul Jensen,Y.B. Zhang, F.X. Lin, Z.Q. Zhang, Q. Liu, Scripta Mater. 67 (2012) 320-323

[30] O. Engler, V. Randle, Introduction to Texture Analysis: Macrotexture, Microtexture and Orientation Mapping, 2nd ed., CRC Press, Boca Raton FL, 2010

[31] W.C. Liu, H. Yuan, M.J. Huang, Metall. Mater. Trans. 40A (2009) 2794-2797

[32] O. Engler, P. Yang, X.W. Kong, Acta Mater. 44 (1996) 3349-3369

[33] O.V. Mishin, D. Juul Jensen, N. Hansen, Metall. Mater. Trans. 41A (2010) 2488-2497

[34] O. Engler, Mater. Sci. Technol. 12 (1996) 859-872.

[35] O.V. Mishin, A. Godfrey, D. Juul Jensen, N. Hansen, Acta Mater. 61 (2013) 5354-5364

[36] J.-H. Ryu, D.N. Lee, Mater. Sci. Eng. A 336 (2002) 225-232

[37] C. Schäfer, J. Song, G. Gottstein, Acta Mater. 57 (2009) 1026-1034

[38] J.J.Sidor, R.H.Petrov, L.A.I.Kestens, Acta Mater. 59 (2011) 5735-5748

[39] N.Hansen. Acta Metall. 25 (1977) 863-869

[40] M.F. Ashby, in: AIME Conference Proceedings, New York Meeting Society, New York, 1966.

[41] A.M.F.Muggerud, E.A.Mørtsell, Y.J Li, R.Holmestad, Mater. Sci. Eng. A 567 (2013) 21–28.

[42] X. Huang, N. Hansen, N. Tsuji, Science 312 (2006) 249–51

[43] Y. Birol, Scripta Mater. 59 (2008) 611-614

[44] N.V. Govindaraj, R. Bjørge, B. Holmedal, Metall. Mater. Trans. 45A (2014) 1597-1608

[45] F.J. Humphreys, M.G. Ardakani, Acta Mater. 44 (1996) 2717-2727

[46] K. Barmak, J. Kim, C.-S. Kim, W.E. Archibald, G.S. Rohrer, A.D. Rollett et al., Scripta Mater. 54 (2006) 1059-1063

[47] J. Li, S.J. Dillon, G.S. Rohrer, Acta Mater. 57 (2009) 4304-4311

[48] D. Raabe, K. Lücke, Scripta Mater. 26 (1992) 19-24

[49] H.-K. Park, J.-H. Kang, C.-S. Park, C.-H. Han, N.-M. Hwang, Mater. Sci. Eng. A 528 (2011) 3228-3231

[50] Q. Zeng, X. Wen, T. Zhai, Metall. Mater. Trans. 40A (2009) 2936-2948

[51] W.C. Liu, J.G. Morris, Scripta Mater. 54 (2006) 2095-2099

[52] E. Hersent, K. Huang, J. Friis, K. Marthinsen, Mater. Sci. Forum 753 (2013) 143-146